International Journal of Radiation Oncology biology • physics

www.redjournal.org

Physics Contribution

# Real-Time Infrared Motion Tracking Analysis for Patients Treated With Gated Frameless Image Guided Stereotactic Radiosurgery

**R. Lee MacDonald, PhD,* Young Lee, PhD, MIPEM,* Jannie Schasfoort, MSc,† Hany Soliman, MD, FRCPC,* Arjun Sahgal, MD, FRCPC,* and Mark Ruschin, PhD, MCCPM***

**Department of Radiation Oncology, Sunnybrook Health Sciences Centre, University of Toronto, Toronto, Ontario, Canada; and †Gamma Knife Center Tilburg, ETZ Hospital, Tilburg, Netherlands*

Received Jul 22, 2019, and in revised form Sep 24, 2019. Accepted for publication Oct 18, 2019.

**Purpose:** The transition from frame-based brain stereotactic radiosurgery (SRS) to frameless delivery is supported by real-time intrafraction monitoring to ensure accurate delivery. The purpose of this study is to characterize these real-time motion traces in a large cohort of patients treated with frameless gated brain SRS and to develop patient-specific predictions of tolerance violations.

**Methods and Materials:** SRS patients treated on the Gamma Knife Icon were immobilized using a device-specific thermoplastic head mask. A motion marker was fixed to the patient's nose, with gating and cone beam computed tomography (CBCT)-based corrections to the treatment at excursions from baseline exceeding 1.5 mm. The traces of 1446 fractions were analyzed according to magnitude (932 unique treatment plans for 462 unique individual patients), directional distribution of displacement, and stability. A neural network model was developed to predict interruptions based on a subset of trace data.

**Results:** The average displacement of the marker in the first fraction of all patients was $0.62 \pm 0.25$ mm with beam CBCT corrections, which would otherwise be modeled at $0.96 \pm 0.96$ mm without intrafraction motion correction ($P < .0001$). Twenty-nine percent of fractions delivered were interrupted, of which the Z-axis (superoinferior) motion was the largest contributor to excursion. Baseline corrections significantly compensated for the magnitude of motion in all 3 dimensions ($P < .01$). The motion relative to the first acquired CBCT was on average seen to consistently increase with treatment time, with the minimum $P$ value occurring at 61.3 minutes. The neural network prediction model was able to predict treatment interruptions with 84% sensitivity on the first 5-minute sample of the trace.

**Conclusions:** Corrections to marker position significantly decreased marker excursions in all 3 axes compared with a single CBCT alignment. Patient-specific modeling may aid in the optimization of cases selected for frameless radiosurgery to increase the accuracy of planned delivery. 

Corresponding author: R. Lee MacDonald, PhD; E-mail: Lee.MacDonald@sunnybrook.ca

Disclosures: A.S. has received honoraria for educational seminars and receives a research grant from Elekta Instrument AB. M.R. is the co-inventor of and owns associated intellectual property specific to the image-guidance system on the Gamma Knife Icon. R.L.M. is co-inventor of and owns associated intellectual property for stereotactic radiosurgery dose optimization algorithms with Brainlab AG. H.S. has received honoraria for speaking engagements from Elekta.

Int J Radiation Oncol Biol Phys, Vol. 106, No. 2, pp. 413–421, 2020

https://doi.org/10.1016/j.ijrobp.2019.10.030

## Introduction

The transition of stereotactic radiosurgery (SRS) delivery from frame-based delivery to noninvasive immobilization using thermoplastic mask fixation has enabled single-fraction delivery and hypofractionated multiday treatments.[1] Although both systems allow submillimeter patient intrafraction motion, noninvasive immobilization in SRS has been shown to have larger motions in all axes.[2-4] Motion during frameless SRS may affect dosimetric quality by reducing conformity.[5]

The Gamma Knife Icon (GKI)[6] system (Elekta AB, Stockholm, Sweden) is a novel evolution of the Gamma Knife (GK) frame-based system. It uses an on-board cone beam computed tomography (CBCT) to verify positioning before treatment and a real-time tracking system using a reflective nose-marker as a surrogate of target motion relative to the CBCT baseline.[6-8] When deviations are detected, the treatment is gated, and CBCT scans are acquired to re-establish baseline. The accuracy of the marker tracking system has been shown to be **sub-0.1 mm**.[6,9-11] The 3-dimensional (3D) motion data are captured as a log-file together with temporal information about the treatment and CBCT acquisitions.

Because the transition from frame to mask-based immobilization is a paradigm shift in SRS, and in particular in the GK community, there are limited data on patient tolerability and immobilization accuracy. Although there have been published abstracts in patient series (with $N \leq 100$),[12,13] a motion characterization model based on a comprehensive patient series with direction-specific analyses would further the understanding of trends in accuracy and tolerability.

In the present study we characterize a large ($N = 462$ patients) population of traces from the GKI that encompasses 1446 unique traces using novel data extraction and analysis methods. This study is the first to identify trends in directionality of intrafraction motion, establish the dependency of motion on treatment duration, stratify populations based on model-defined thresholds, and generate a predictive model for deviations from baseline on the GKI system.

## Methods and Materials

### Coordinate system nomenclature

Intrafraction motion monitoring tracks the position of an infrared marker placed on the nose (referred to hereafter as *marker*) with respect to fixed markers on the mask adapter at 20 Hz and displays the 3D magnitude of the vector offset from baseline on the console of the GKI.[6] The log-file saves localization data if the total magnitude of motion of the marker is 0.2 mm or greater relative to the previous marker position.[6] This coordinate is the raw stereotactic data at a point, *P,* defined herein as:

$$P^{raw} = [x^{raw}, y^{raw}, z^{raw}]$$

Before treatment, CBCT scans provide the reference localization positioning of the patient for treatment adaptation. To provide context for the marker data, the 3D magnitude vector value of the marker position when the first reference point has been approved via CBCT is recorded, defined herein as:

$$P^0 = [x^0, y^0, z^0]$$

This point is referred to as the *first approved reference point* and converts 3D magnitude vector raw marker data to motion relative to the accepted baseline. The raw data converted to be relative to the first approved reference point is defined herein as *relative position*:

$$\boldsymbol{P^{rel}} = \boldsymbol{P^{raw}} - \boldsymbol{P^0} = [\boldsymbol{x^{raw}} - \boldsymbol{x^0}, \boldsymbol{y^{raw}} - \boldsymbol{y^0}, \boldsymbol{z^{raw}} - \boldsymbol{z^0}] = [\boldsymbol{x^{rel}}, \boldsymbol{y^{rel}}, \boldsymbol{z^{rel}}]$$

Throughout the treatment, the approved reference point can be updated by additional CBCT scan s to re-establish baseline position as

$$P^t = [x^t, y^t, z^t]$$

The positional information relative to the first approved reference point has been defined as $\boldsymbol{P^{rel}}$ The raw position updated by all approved reference points at the time of acquisition, defined as the *corrected position,* herein is

$$\boldsymbol{P^{cor}} = \boldsymbol{P^{raw}} - \boldsymbol{P^t} = [\boldsymbol{x^{raw}} - \boldsymbol{x^t}, \boldsymbol{y^{raw}} - \boldsymbol{y^t}, \boldsymbol{z^{raw}} - \boldsymbol{z^t}] = [\boldsymbol{x^{cor}}, \boldsymbol{y^{cor}}, \boldsymbol{z^{cor}}].$$

The distinction between $\boldsymbol{P^{cor}}$ and $\boldsymbol{P^{rel}}$ is useful to identify differences between marker motion during treatment and marker motion relative to the corrections made by the system using approved reference points. It is important to note that before a re-established baseline, usually caused by an intrafraction motion interruption event, $\boldsymbol{P^{cor}} = \boldsymbol{P^{rel}}$. The total displacement, *r,* is calculated from the magnitude of the vector offset from the baseline as

$$r = \sqrt{x^2 + y^2 + z^2}$$

The difference between relative and corrected displacements is illustrated in Figure 1, with the 2 values coinciding after the first approved reference point but separating after the second CBCT acquisition at approximately 33 minutes and the proceeding update to the approved reference point. The blue and red shaded regions in Figure 1 indicate the period of beam-on for the CBCT and the treatment beam, respectively.

From Figure 1, we can also see that the beginning of the marker position analysis coincides with the acceptance of the first approved reference point. Although there is marker positional information before this time point, it has no accepted baseline information and therefore should not contribute to the analysis.

## Motion trace metrics

### Time-weighted average displacement

Given motion trace information, the time-weighted average displacement was calculated by:

$$\overline{D}_r = \frac{1}{t}\int_0^t r\,dt \quad (1)$$

where $r$ is the magnitude of the vector displacement and $t$ is the total trace time. For all instances of this metric in this study, $\overline{D}$ is measured only over the period of treatment beam-on. This was done to prevent the inclusion of nose marker deviations during CBCT, patient setup, or excursions during beam-off because these would not contribute to dosimetric impact.

### Markers per second

Because the marker position is only reported if the corrected position deviates by more than 0.2 mm, sampling of marker position in the log-file is not uniform with respect to time. As such, the number of markers per unit time is an indication of the relative stability of a given trace. The marker per second (MPS) metric was calculated as

$$MPS = \frac{N}{t} \quad (2)$$

where $N$ is the number of recorded marker positions between the time of the first approved reference point and the end of the last treatment beam, and $t$ is the time between first approved reference point and the last beam-off.

### Treatment interruption

An interruption is defined by the movement of the sources to the off-position with the detection of large movements of the marker above a threshold.[6] This threshold for motion was defined at our institution to be 1.5 mm (total magnitude vector). Treatment interruptions are indications of motion and may create extended treatment times with the requirement for additional CBCT scans and re-establishment of baseline. An example of an interruption is shown graphically Figure 1, just before 30 minutes.

## Population of motion traces

The database of treatment log-files from our institution over an 18-month period was imported to MATLAB (MathWorks 2018b) using an in-house executable. Additional in-house software was used to parse and define every motion trace according to its treatment context by cross-referencing the clinical database. One fraction from each unique individual in the database was used, removing any bias from repeated measuring of metrics using the same individuals' multiple fractions.

The database included 1446 unique traces, constituting 932 unique plans, for 462 unique patients. The previously defined metrics were used to analyze all motion traces to generate overall population statistics. One fraction (the first fraction) from every patient was analyzed to avoid oversampling individuals (N = 462). Intrapatient analyses were performed by examining all fractions of patients with more than 1 delivery (N = 282).

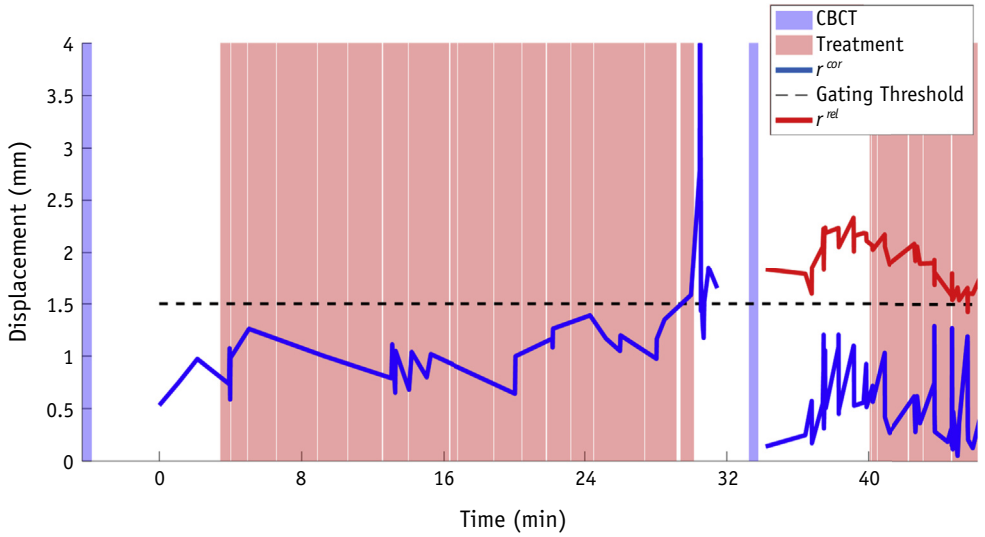


**Fig. 1.** Visualization of the log-file information for a Gamma Knife Icon treatment using the infrared motion management (IFMM). The time is relative to the first approved reference point that was accepted. The shaded blue region indicates the period of cone beam computed tomography acquisitions. The shaded red regions indicate the period of treatment beam-on. The solid blue line indicates the position of the IFMM relative to all approved reference points, the solid red line indicates the position of the IFMM relative to the first approved reference point, and the dotted black line indicates the gating threshold of 1.5 mm relative to baseline.

The metrics described were used to analyze the population of traces. The *MPS* and time-weighted average displacement for the corrected ($\overline{D}_r^{cor}$) and relative ($\overline{D}_r^{rel}$) were measured for all traces. In addition, each axis (*X, Y,* and *Z*) was also examined independently (eg, for X-axis, $\overline{D}_x^{rel}$ and $\overline{D}_x^{cor}$). Treatment duration was also tabulated and compared with these metrics to identify any interdependency.

Additionally, interpatient and intrapatient statistics were compared to assess the degree to which these metrics are characteristic for a given patient. The mean, $\mu$, is the average of all deviations averaged over every fraction (N = 462); the intrafraction standard deviation, $\sigma_{intra}$, is the root mean square of the standard deviations of each multifraction case (N = 282); and the interpatient standard deviation, $\sigma_{inter}$, is the standard deviation of all deviations averaged over every fraction (N = 462).

## Classification of data and prediction of interruption

To identify trends, all cases were analyzed using the defined metrics for interdependence. Of particular focus was the occurrence of treatment interruptions. Traces were stratified by whether there was an interruption, and the groups were analyzed for dependency of metrics.

The dependence of treatment interruption on metrics was also tested by submitting metrics measured on subsamplings of the traces to the MATLAB neural network toolbox (MathWorks). MATLAB's pattern recognition tool was trained on 400 randomly selected cases using scaled conjugate gradient backpropagation[14,15] with 10 hidden layer neurons. We conducted preliminary experiments to develop the network training approach. Ten hidden layers were used to balance the time of training in MATLAB with the performance of the results output from the model. Fifty random cases were used to test the neural network. Four hundred training cases and 50 test cases were chosen so that only 1 trace per unique individual was used to maximize the size of the training set, while maintaining a large enough test population for meaningful results (this presents an 89% to 11% split of training to testing data). Metrics measured on the first 300 seconds of the trace were tested for their ability to predict whether the trace would contain an interruption during treatment. The decision to use 300 seconds (5 minutes) was a balance between requiring sufficient data for training while still being short enough for prompting clinical interventions. Our mean treatment time is 46 minutes, so catching an unstable setup within the first 5 minutes could be useful. At less than 5 minutes the results of some preliminary investigations indicated that the model would not be as stable.

## Results

The distribution of magnitude vector time-weighted average displacement for the corrected ($\overline{D}_r^{cor}$) and relative ($\overline{D}_r^{rel}$) marker positions are shown in Figure 2A and 2B, respectively. The distribution of corrected data (Fig. 2A) is maintained below 1.5 mm, by definition, through the clinical gating threshold.

By separating the beam-on marker data into directions, histograms were produced that show the marker position as a function of deviation from baseline with and without the CBCT corrections, plotted in Figure 3. The intrafraction CBCT corrections reduce motion and center the distribution in all directions ($P < .01$). The corrected data show that the most frequent motion was in the Z-axis (superoinferior direction), followed by the Y-axis (anteroposterior), with the X-axis (lateral) having the least motion (as seen in standard deviation differences in Fig. 3).

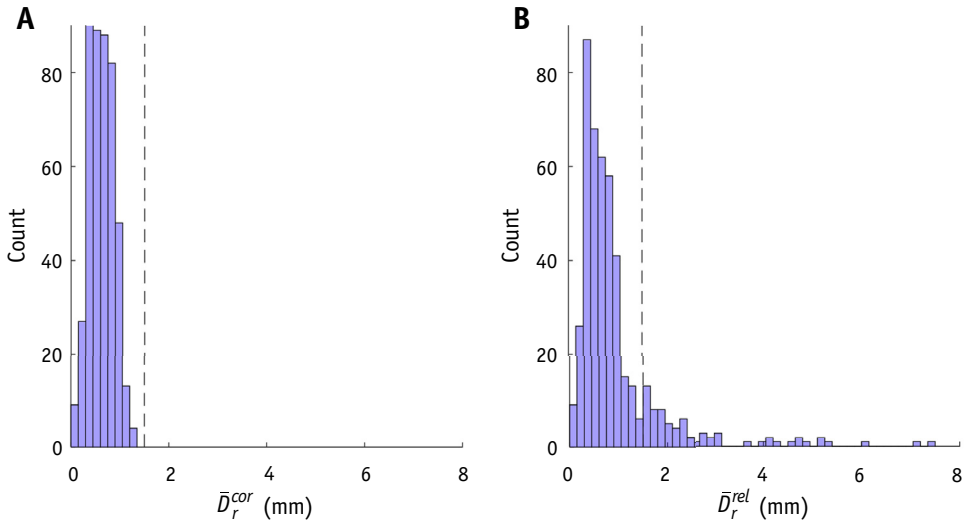


**Fig. 2.** Population histogram of time-weighted average displacement (N = 462). (A) The histogram of displacements corrected by all approved reference points. (B) The histogram of displacements corrected by the first approved reference point. The dashed line indicates the threshold of 1.5 mm used clinically for gating.

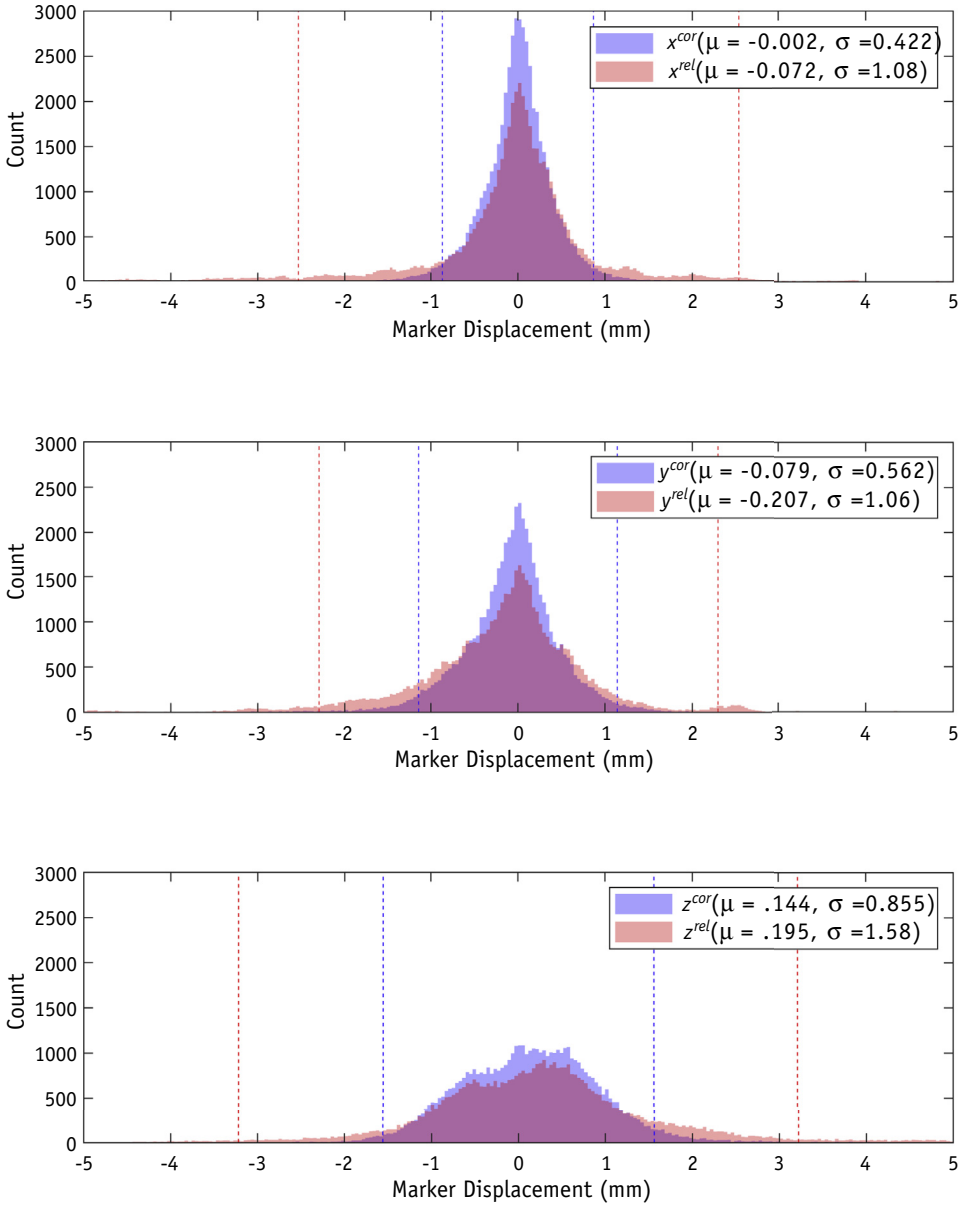


**Fig. 3.** Histograms of the marker position during beam-on for each of the axes of motion. The red data are the motion traces relative to the first approved reference point. The blue data are motion traces corrected by all approved reference points. The dashed lines indicate the range of the 95th percentile of relative and corrected data shown in red and blue, respectively.

Table 1 shows the comparison of mean, interpatient, and intrapatient standard deviation of the relative time-weighted average deviation and ***MPS*** metrics across all cases. From these values we can see that the deviations between patients is notably higher than within the same patient for $\overline{\boldsymbol{D}}_{\boldsymbol{y}}^{\boldsymbol{rel}}$, $\overline{\boldsymbol{D}}_{\boldsymbol{z}}^{\boldsymbol{rel}}$, and $\overline{\boldsymbol{D}}_{\boldsymbol{r}}^{\boldsymbol{rel}}$, indicating a potential for the detection of patient-specific characteristics with these metrics.

## Treatment interruption

The statistics of treatment interruptions for all fractions (N = 1446) indicate that 29% of cases had at least 1 interruption in their treatment, and 18% had more than 1. When further stratifying the deviations causing interruption, the Z-axis was the primary contributor to deviations from baseline in 72% of interruptions, with the Y-axis as the secondary contributor in 51% of interruptions. The X-axis was the primary contributing axis in only 15% of interruptions.

The prediction of treatment interruptions can work to reduce overall treatment time. Figure 4 shows the magnitude vector relative time-weighted average deviation averaged across all patients. On average, the tendency is for this relative deviation to increase with increasing treatment time. This trend highlights the need to minimize treatment

**Table 1** Summary statistics of the mean, intrapatient, and interpatient values for relative axis-specific time-weighted deviations

| | μ | $\sigma_{intra}$ | $\sigma_{inter}$ |
|---|---|---|---|
| $\overline{D}_x^{rel}$ | 0.432 | 0.549 | 0.515 |
| $\overline{D}^{cor}$ | 0.470 | 0.471 | 1.370 |
| $\overline{D}_z^{rel}$ | 0.755 | 0.684 | 2.711 |
| $\overline{D}_r^{rel}$ | 1.124 | 0.903 | 3.064 |
| ***MPS*** | 0.068 | 0.104 | 0.107 |

μ is the average of all deviations averaged over every fraction, $\sigma_{intra}$ is the root mean square of the standard deviations of each multifraction case (N = 282), and $\sigma_{inter}$ is the standard deviation of all deviations averaged over every fraction.

time and prevent dosimetric deterioration associated with intrafraction motion. Additionally, this trend indicates that the longer the treatment is extended, the more corrective CBCT scans will be required.

## Classification of data and prediction of interruption

The first fraction from each individual patient in the database was used to form 2 groups: those with treatment duration below and above a given value. This value was transitioned over the range of durations, with statistical analysis performed at each stage. The minimum $P$ value separating the 2 populations ($P < .001$) was found to be at $t = 61.3$ minutes, producing a separation of $\overline{D}_r^{rel} = 0.96$ mm. A number of traces (1078) had treatment durations less than this threshold, and 358 traces had treatment durations greater than this threshold. The average and standard deviation for the entire population of traces (N = 1446) was 46.41 minutes and 35.12 minutes, respectively.

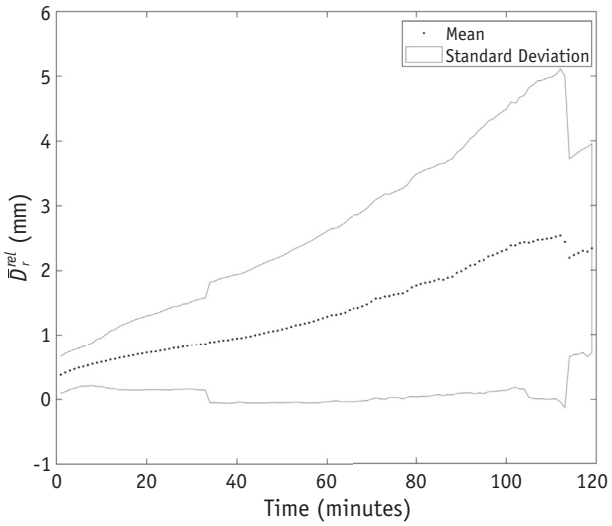


**Fig. 4.** Average and standard deviation of the relative time-weighted average deviation computed every minute for 1446 fractions.

A histogram similar to the entire population of 1446 motion traces is shown in Figure 5A, separated into groups: with and without interruption. The natural log of ***MPS*** (likely to be an indication of patient-exhibited instability) for populations with and without treatment interruption is shown in Figure 5C. Separation of both of these populations is statistically significant at $P < .01$. By thresholding this population by the intersection point of the normal distributions for the 2 populations we can produce quadrants that separate the traces into categories based on likelihood of interruption. Only 3.8% of traces that interrupted were found in the lower left quadrant ($ln[MPS] < -3.5$ and $\overline{D}_r^{cor} > 0.7$ mm), and 64.5% of cases that interrupted were found in the upper right quadrant ($ln[MPS] < -3.5$ and $\overline{D}_r^{cor} > 0.7$ mm), although it contained only 8.6% of uninterrupted traces.

By implementing the MATLAB neural network package trained on a population of 400 cases from unique patients, prediction receiver operating characteristic area under the curve (AUC) of the presence of interruption in a given fraction, based on the first 5 minutes of the same fraction's trace, had a value of 0.84 on a population of 50 independent cases. This AUC value indicates the network was capable of predicting a notable portion of the patients from a short subsampling of the motion trace data.

## Discussion

In the present study, we have characterized motion for a large (N = 462 patients) population treated on the GKI. From Figures 1, 2, and 3, it is clear that the corrections to baseline from the intrafraction motion system are significantly effective ($P < .01$) at reducing the time-weighted average deviation from baseline. One study has shown that, on average, intracranial targets are displaced by approximately half the magnitude of the marker.[16] This suggests that limiting the motion of the nose marker is likely to also reduce target motion, although a thorough validation to determine the degree to which this is true has not yet been conducted. More can also be incorporated regarding how the predictions facilitated by this work would be best employed clinically. For example, if interruptions are to be avoided in part because they prolong treatment, which can compromise the integrity of the plan's dosimetry, to what degree is that preferable to the proposed technique of increasing margins to avoid the interruption? In addition, false positives and false negatives in these predictions may lead to different dosimetric consequences.

Figure 3 shows the directional dependence of intrafraction motion during GKI treatments. The superoinferior direction has a larger magnitude of average motion and is responsible for the majority of interruptions. These data may potentially inform refinements to noninvasive

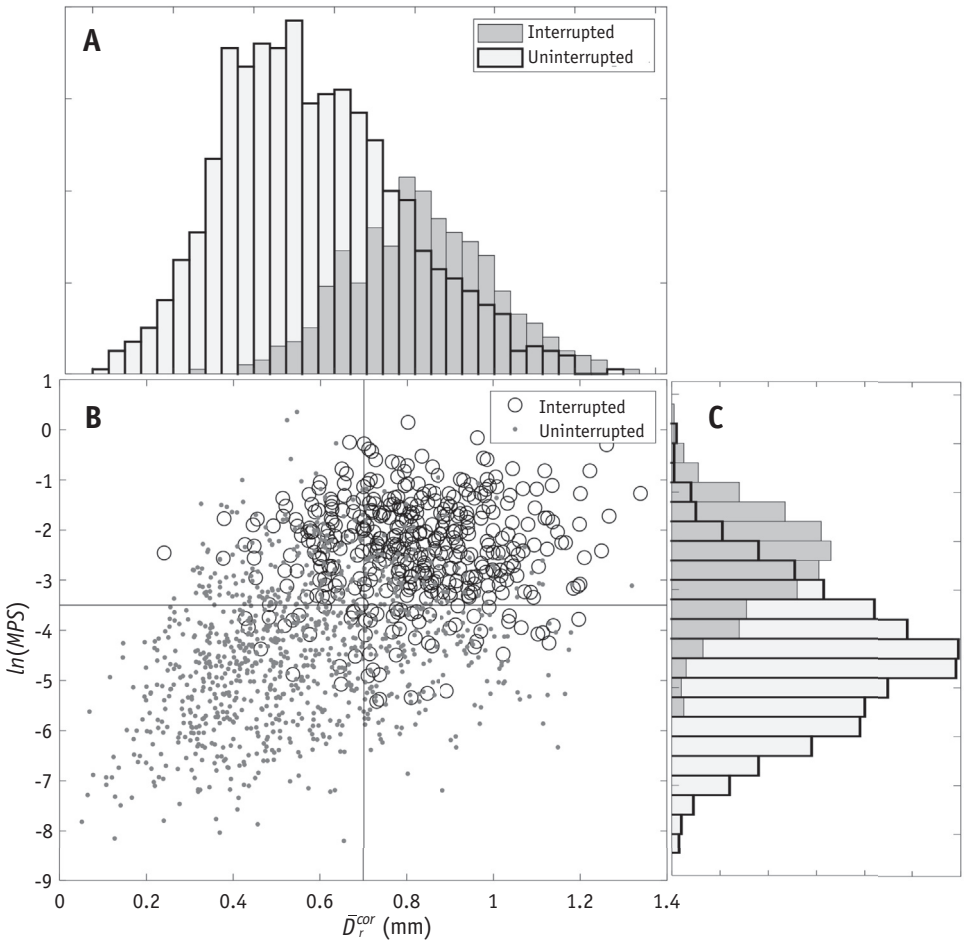


**Fig. 5.** Stratification of the population of cases into quadrants that characterize the likelihood of interruption given the stratification of motion trace via 2 analysis metrics. Distribution shown in (A) and quantified on the horizontal axis in (B) is the time-weighted average deviation corrected by all approved reference points. The distribution shown in (C) and quantified on the vertical axis in (B) is the natural-log of the number of nose marker positions registered in the log-file per second of treatment.

immobilization to increase the rigidity specifically in this direction of motion.

Table 1 compares intra- versus interpatient data over the population of cases. There are notable differences in the variation between individuals relative to those for repeated measurements of the same individual in the superoinferior, anteroposterior, and magnitude vector directions. These reduced intrapatient variations have potential as a means of identifying the characteristic stability of a given patient before treatment. Identifying patient-specific motion characteristics could contribute to the creation of patient-specific margin design for treatment planning, if correlated with the target volume, by accounting for anticipated motion during treatment.

Figure 5 shows that the treatments possessing interruptions can be successfully stratified based on population thresholds of the corrected time-weighted average deviation, $\overline{D}^{cor}$, and the number of markers per second, *MPS*. Furthermore, metrics calculated on subsamples of a trace show high correlation with the metrics computed for the complete trace. This suggests that patients' motion performance shows some consistency over the course of treatment. The use of neural networks to generate predictions about future interruptions shows a high level of accuracy, and incorporating additional metrics as input to the neural network could further improve its performance.

In terms of clinical applicability, such a prediction model can be incorporated into a clinical workflow as a tool of real-time analysis to identify motion traits suggesting future interruptions, allowing therapy staff to take steps to mitigate deviations before their occurrence. Additionally, a short acquisition of motion data may inform decisions about expected performance during treatment. One clinical embodiment of this could be an acquisition of a 5-minute sample of motion taken in the immobilization mask at the time of simulation. This short trace could then be analyzed for the metrics shown in this study and supplied to the neural network for prediction. Refinement of the neural network with a larger population of traces and metrics that

yield increased sensitivity and specificity may yield superior results and will be the focus of future work. Combined with correlating information between the nose marker and the target volume, this could additionally contribute to decisions regarding the requirement of additional care/sedation or patient-specific margins. The AUC value for the neural network output had a higher value than that for the input metrics independently. With further refinement, it will be explored whether these metrics alone provide sufficient value as a predictor.

A limitation of this study is that no rotational information was included in the model due to the nature of the collected motion trace. Additionally, all motion is motion of the nose marker, not the target volume. All information regarding interruptions and patient treatment context were programmatically extracted. As such, we expect minor misclassifications, which can be further improved through refining methods of detecting typical clinical scenarios. As previously mentioned, the trace was sampled each time the marker displaced by 0.2 mm, leaving the possibility that fine motion was not detected. Other clinical factors that may have importance for interpreting traces, including performance status, weight, age, and sedative administration, were not included in the analysis.

Institutions have begun to analyze small populations of intrafraction motion statistics using this information.[12,13] Kim et al[12] report, in an abstract, motion data on 50 patients and find the maximum motion direction to be in the superoinferior direction, with a mean displacement of 0.43 $\pm$ 0.35 mm. Vulpe et al[13] reported, in an abstract, similar results between frameless and framed cohorts for 100 patients. Our series is the largest, with 1446 unique motion traces, constituting 932 unique treatment plans, for 462 unique individual patients, with the ability to determine trends in the directionality of the observed intrafraction motion. Furthermore, we have incorporated automated analysis and methods for characterizing the spectrum of performance in the immobilization system and predicting the performance of patients. Predictions may lead to the prevention of dosimetric impact of intrafraction motion.

It is important to stress that, at the present time, treatment using a mask with this SRS technology, in conjunction with motion tracking and image guidance, is still a relatively new paradigm for most users. As such, limited data have been reported regarding how well the mask immobilizes patients over time, the spread in patient tolerance of the mask, and ultimately the thresholds that should be used for gating treatments and performing baseline corrections. How the intracranial target moves in the mask in relationship to how the nose moves ultimately must be addressed for patient-specific thresholds, and this question requires modeling of the head. This subject is currently being investigated as future work by our group and others.[16] The goal of the present paper was to quantify the immobilization and tolerability of the masks.

The clinical applicability of our work is 3-fold. First, we have assembled large-scale data on the directionality of motion within the mask. Although it may not be surprising that craniocaudal motion is the dominant direction based on our clinical experience, evidence-based validation of our clinical assumption is important and can be used to motivate future work or initiatives to improve the mask's immobilization performance in that direction. Second, although it was also suspected that longer treatments yield increased probability of decreased tolerance, our study clearly demonstrates this with data. In Figure 5, it is clear that motion itself increases with increasing treatment time, which provides clinicians with needed information when weighing and balancing treatment time against other parameters when planning a patient case. Third, our preliminary modeling work shows that one can predict whether a patient will come out of tolerance by monitoring the patient for 5 minutes.

We could use these findings in several ways. Consider the example of a complex case that may require hours of treatment—for example, a patient with 30 brain metastases to be treated with single-fraction SRS. At our institution we would apply our spatially partitioned adaptive radiosurgery technique, which treats targets daily; the number of targets is determined by a maximum treatment time of 60 minutes. We recently reported the technical details of our spatially partitioned adaptive radiosurgery technique and potential dosimetric advantages compared with hippocampal-avoidance whole brain radiation therapy.[17] In this clinical situation, a mock 5-minute immobilization to test the potential of successful treatment would be ideal before starting the treatment process. If, within the 5-minute mock immobilization, the prediction model tells us there is a high possibility of unacceptable movement, other forms of treatment could be considered. For example, a decision may be made to perform frame-based SRS on the Icon or to seek an alternative technology such as linear accelerator−based SRS with image guidance, robotic technology for positional corrections, and fast-dose-rate and/or volumetric modulated arc therapy capability. Therefore, these data have the potential to allow for data-driven decisions in terms of the ideal technology for the patient and treatment approach. In fact, this study was motivated by observations that we have encountered in the clinic, such as the aforementioned clinical scenario, and our future directions include applying this 5-minute mock procedure in our clinical workflow.

Future work will be aimed at correlating the marker deviations with target deviations to quantify the dosimetric benefit of maintaining the marker at baseline. Additional focus will be given to developing metrics that attempt to further identify variation within a given patients' fractions relative to different patients to characterize the consistency of patients' motion from fraction to fraction. This can also aid in the development of neural networks for predicting patient performance on future fractions on the basis of the current fraction. Finally, this work will incorporate predicted motion into inverse optimization with the aim of creating additional robustness for treatments likely to

involve substantial motion. This optimization could aim to minimize the degradation of plan quality with the characterized motions shown in this study.

## Conclusions

The statistical analysis of real-time tracking information from patients treated on the GKI can provide insight into the clinical tolerability and stability of treatments. The superoinferior dimension tends to show the highest magnitude of deviation. Deviation from an initial baseline tends to increase, on average, throughout treatment. Motion trace statistics tended to have less variation from fraction to fraction for the same individual compared with between individuals. Correlation of target motion with the real-time tracking of the nose marker will allow for dosimetric error approximation.

## References


1. Myrehaug S, Soliman H, Tseng C-L, Ruschin M, Larson D, Sahgal A. Why hypofractionate stereotactic radiosurgery for brain metastases? *CNS Oncol* 2016;5:111-113.
2. Carminucci A, Nie K, Weiner J, Hargreaves E, Danish SF. Assessment of motion error for frame-based and noninvasive mask-based fixation using the Leksell Gamma Knife Icon radiosurgery system. *J Neurosurg* 2018;129:133-139.
3. Babic S, Lee Y, Ruschin M, et al. To frame or not to frame? Cone-beam CT-based analysis of head immobilization devices specific to linac-based stereotactic radiosurgery and radiotherapy. *J Appl Clin Med Phys* 2018;19:111-120.
4. Chung H-T, Park W-Y, Kim TH, Kim YK, Chun KJ. Assessment of the accuracy and stability of frameless gamma knife radiosurgery. *J Appl Clin Med Phys* 2018;19:148-154.
5. Guckenberger M, Roesch J, Baier K, Sweeney RA, Flentje M. Dosimetric consequences of translational and rotational errors in frameless image-guided radiosurgery. *Radiat Oncol* 2012;7:63.
6. Elekta Instrument AB. High definition motion management - enabling stereotactic Gamma Knife® radiosurgery with non-rigid patient fixations. Stockholm, Sweden: White Paper; 2015.
7. Ruschin M, Komljenovic PT, Ansell S, et al. Cone beam computed tomography image guidance system for a dedicated intracranial radiosurgery treatment unit. *Int J Radiat Oncol Biol Phys* 2013;85:243-250.
8. Stieler F, Wenz F, Abo-Madyan Y, et al. Adaptive fractionated stereotactic Gamma Knife radiotherapy of meningioma using integrated stereotactic cone-beam-CT and adaptive re-planning (a-gkFSRT). *Strahlenther Onkol* 2016;192:815-819.
9. Burton K. End-to-end testing of the Leksell Gamma Knife Icon system. Available at: https://smartech.gatech.edu/handle/1853/59298. Accessed May 22, 2019.
10. Sarfehnia A, Ruschin M, Chugh B, et al. Performance characterization of an integrated cone-beam CT system for dedicated gamma radiosurgery. *Med Phys* 2018;45(9):4179-4190.
11. Li W, Bootsma G, Von Schultz O, et al. Preliminary evaluation of a novel thermoplastic mask system with intra-fraction motion monitoring for future use with image-guided Gamma Knife. *Cureus* 2016;8:e531.
12. Kim JO, Fallon K, Bednarz G, et al. Patient motion analysis of first 50 frameless fixation cases with Leksell Gamma Knife ICON. *Int J Radiat Oncol Biol Phys* 2018;102:e495-e496.
13. Vulpe H, Elliston C, Xu Y, et al. Frameless stereotactic radiosurgery on the Gamma Knife ICON: First 100 consecutive patients. *Int J Radiat Oncol Biol Phys* 2019;103:E29.
14. Møller MF. A scaled conjugate gradient algorithm for fast supervised learning. *Neural Networks* 1993;6:525-533.
15. Bishop CM. *Neural Networks for Pattern Recognition.* Ohio: Oxford University Press, 1995.
16. Wright G, Schasfoort J, Harrold N, Hatfield P, Bownes P. Intra-fraction motion gating during frameless Gamma Knife® Icon™ therapy: The relationship between cone beam CT assessed intracranial anatomy displacement and infrared-tracked nose marker displacement. *J Radiosurg SBRT* 2019;6:67-76.
17. Nguyen TK, Sahgal A, Detsky J, et al. Single-fraction stereotactic radiosurgery versus hippocampal-avoidance whole brain radiation therapy for patients with 10 to 30 brain metastases: A dosimetric analysis. *Int J Radiat Oncol Biol Phys* 2019;105:394-399.